Electronic Supplementary Information

Mn-incorporated nickel selenide: an ultra-active bifunctional electrocatalyst for hydrogen evolution and urea oxidation reactions

Meysam Maleki[a], Ghasem Barati Darband[b*], Alireza Sabour Rouhaghdam[a], Reza Andaveh[a]

Zahra Mohammadkazemi[a]

[a] Department of Materials Engineering, Faculty of Engineering, Tarbiat Modares University, P.O. Box: 14115-143, Tehran, Iran

[b] Materials and Metallurgical Engineering Department, Faculty of Engineering, Ferdowsi University of Mashhad, Mashhad 91775-1111, Iran

Corresponding author: E-mail: baratidarband@um.ac.ir

Experimental section:

Material synthesis

To preparation of Ni-Mn-Se and Ni-Se electrocatalysts, a potentiostatic electrodeposition method was used. Ni foam was utilized as substrate for all catalysts and was catted with a size of 1×1 cm^{-2} for electrodeposition. Prior to electrodeposition, the Ni foams were degreased in ethanol and marinated in 20 % hydrochloric acid for 15 min and 25 s, respectively. To synthesis of Ni-Mn-Se electrocatalysts, the bath of electrodeposition was consisted of 0.065 M NiCl$_2$.6H$_2$O (Ni ion source), 0.01 M MnCl$_2$.4H$_2$O (Mn ion source), 0.01 M SeO$_2$ (Se ion source), and 0.1 M LiCl (conductivity booster). Potentiostatic electrodeposition was carried out via a three-electrode cell at room temperature, in which, a saturated calomel electrode (SCE) and a platinum electrodes act as reference and counter electrodes, respectively. The potential of -1.2 V vs. SCE for electrodeposition of Ni-Mn-Se electrocatalysts was collected by CV test assistance. To electrodeposition time optimization, the potential remained the same (-1.2 V vs. SCE) and the synthesis times were varying from 5 to 30 min.

By the same electrodeposition parameters, the Ni-Se electrocatalyst was prepared in a bath containing 0.065 M NiCl$_2$.6H$_2$O, 0.01 M SeO$_2$, and 0.1 M LiCl.

Characterization

To explore the morphology of samples, a field emission scanning electron microcopy (FESEM, TESCAN MIRA3) was employed. An energy-dispersive X-ray spectroscope (EDS) was used to study the elemental composition and mapping of Ni, Mn, and Se on the Ni-Mn-Se and Ni-Se electrocatalysts. X-ray diffraction (XRD) and X-ray photoelectron spectroscopy (XPS, Bes Tec Germany) were also utilized to investigate the phase structure and surface chemistry of specimens.

Electrochemical measurements

A SP-300 Bio-Logic potentiostat was employed to carry out all the electrochemical tests. A conventional three-electrode cell, where, graphite and Ag/AgCl were act as the counter and reference electrode, was used for electrochemical performances characterization. Ni foams with the as-prepared electrocatalyst coatings were used as working electrode. The 1.0 M KOH with and without 0.33 M urea was electrochemical tests electrolyte. Moreover, all experiments were done at room temperature. To explore the electrocatalytic activity of specimens the linear sweep voltammetry (LSV) was carried out at the scanning rate of 5 mV s^{-1}. It is worth noting that the each of the LSV measurements was done five time to ensure that the polarization curves are the steady-state ones. The electrochemical impedance spectroscopy (EIS) was performed in the frequency ranging from 100 kHz to 100 mHz to investigate the electrocatalytic kinetics and electrical conductivity of electrocatalysts. Gas bubble evolution was explored via dynamic specific resistance measurements at 870 mV overpotential. To evaluate the long-term electrocatalytic stability of samples, choronopotentiometry tests were carried out at current densities of -200,

200, and 50 mA cm^{-2} for 50 h to examine hydrogen evolution reaction (HER), urea oxidation reaction (UOR), and cell stability. Multi-step choronopotentiometry tests were also performed at current densities of -50 to -300 mA cm^{-2} for HER and 50 to 300 mA cm^{-2} for UOR, where each step was measured for 900 s. The recorded potentials were reported versus the reversible hydrogen electrode (RHE) according to the following Equation S1:

V_{RHE} = V (vs.Ag/AgCl) + V° Ag/AgCl + 0.059 pH   (1)

Calculation of C$_{dl}$, roughness factor (RF), and electrochemically active surface area (ECSA)

Cyclic voltammetry (CV) was employed so as to measure the double-layer capacitance (C$_{dl}$) of electrocatalysts. Therefore, CV test were done at scanning rate ranging from 5 to 120 mV s^{-1} in non-faradic potentials region (-0.45 to -0.55 V vs. SCE). C$_{dl}$ of an electrocatalyst can be measured according to having a linear relationship between the differences in current density between anodic and cathodic (J$_{anodic}$ − J$_{cathodic}$) sweeps and scanning rates.

The ECSA value was calculated according the following formula:

ECSA = C$_{dl}$/C$_s$ (2)

Where, C$_s$ is the flat surface capacitance (40 μF cm^{-2}).

The following equation was used to calculation the (RF) value:

 RF = C$_{dl}$/C$_0$ (3)

Where, C$_0$ is the capacitance of ideal planar metal oxides (i.e. NiO) with smooth surfaces (60 μF cm^{-2})

Calculation of turnover frequency (TOF)

TOF numbers can be calculated from the geometrical substrate surface area and current density at given overpotential during the HER, according to the following formula:

$$TOF = \frac{Total\ Hydrogen\ Turn\ Overs/cm^2\ geometric\ area}{Surface\ active\ sites/cm^2\ geometric\ area}\qquad(4)$$

The total number of evolved hydrogen bubbles can be calculated based on the current density at specific overpotential, according to the following equation:

$$H_2 = (j\frac{mA}{cm^2})(\frac{1C\ s^{-1}}{1000\ mA})(\frac{1\ mol\ e^-}{96485.3\ C})(\frac{1\ mol\ H_2}{2\ mol\ e^-}) \times (\frac{6.022\ \times\ 10^{23}\ H_2\ molecules}{1\ mol\ H_2})$$

$$= \frac{3.12 \times 10^{15} \frac{H_2/s}{cm^2} per \frac{mA}{cm^2}}{} \qquad (5)$$

Assuming that all of the catalytic centers at the surface are participate in the HER, the number of active surface sites can be measured as follows:

$$N = (\frac{4\ atoms}{43.76\ \overset{\circ}{A}})^{2/3} = 9.01 \times 10^{14}\ atoms.cm_{real}^{-2} \qquad (6)$$

Then, the TOF value at each current density can be measured according to the following equation:

$$TOF = \frac{(3.12 \times 10^{15} \frac{H_2/s}{cm^2} per \frac{mA}{cm^2}) \times |j|}{(9.01 \times 10^{14}\ atoms\ cm_{real}^2) \times A_{ECSA}} \qquad (7)$$

Calculation of Gibbs free energy of hydrogen adsorption (ΔG_{H*})

To calculate the ΔG_{H*} on the surface of Ni-Mn-Se and Ni-Se, the density functional theory (DFT) calculations were performed using the Vienna ab inotio simulation package (VASP 5.4.4). The DFT exchange-correlation energy was expressed throughout the generalized gradient approximation (GGA) with Perdew-Burke-Ernzerhof functional. For calculations, two models of Ni-Mn-Se and Ni-Se (111) facets with 9 layers and vacuum widths of 15 A were prepared. The plane wave cutoff was set to 350 eV with a self-consistent field (SCF) tolerance of 1×10^{-6} eV. For structural relaxation, a 4×4×1 k-point grids were adopted and 6 top layers of the models were permitted to be relaxed.
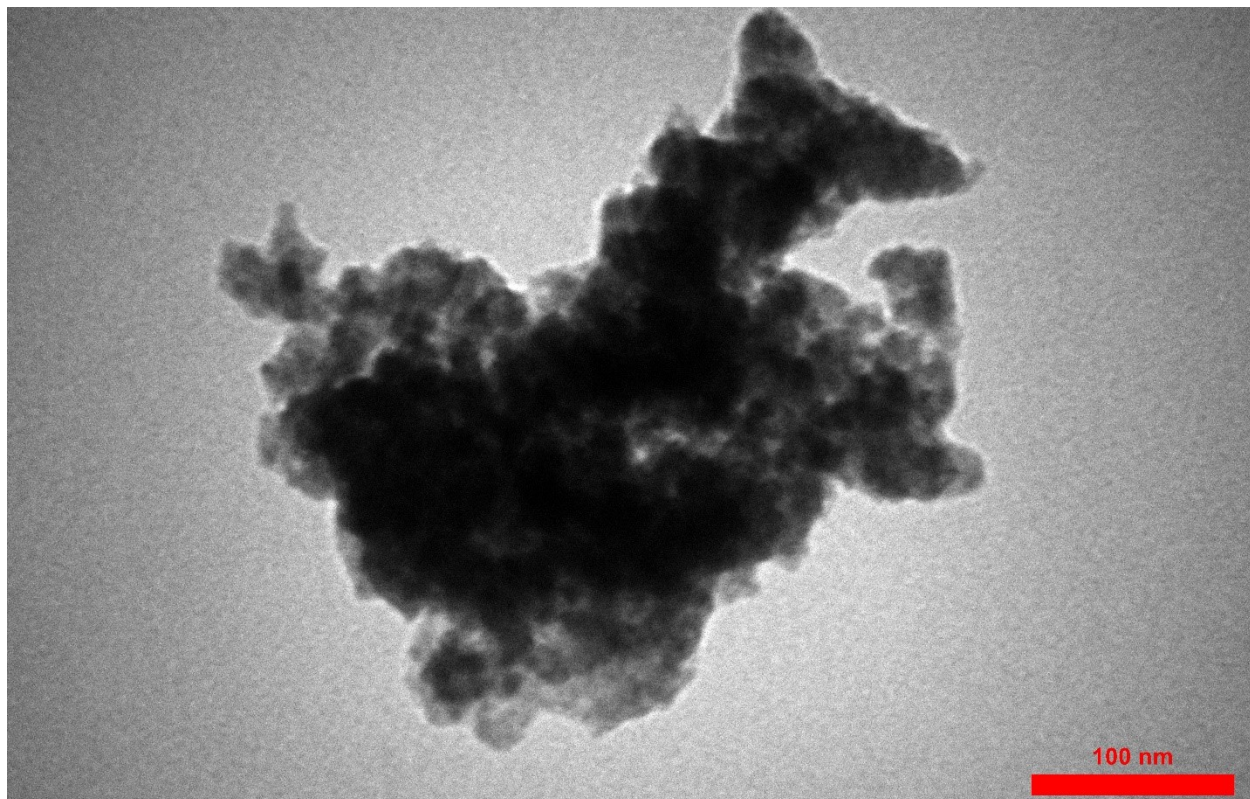
The ΔG_{H*} was calculated as follows:

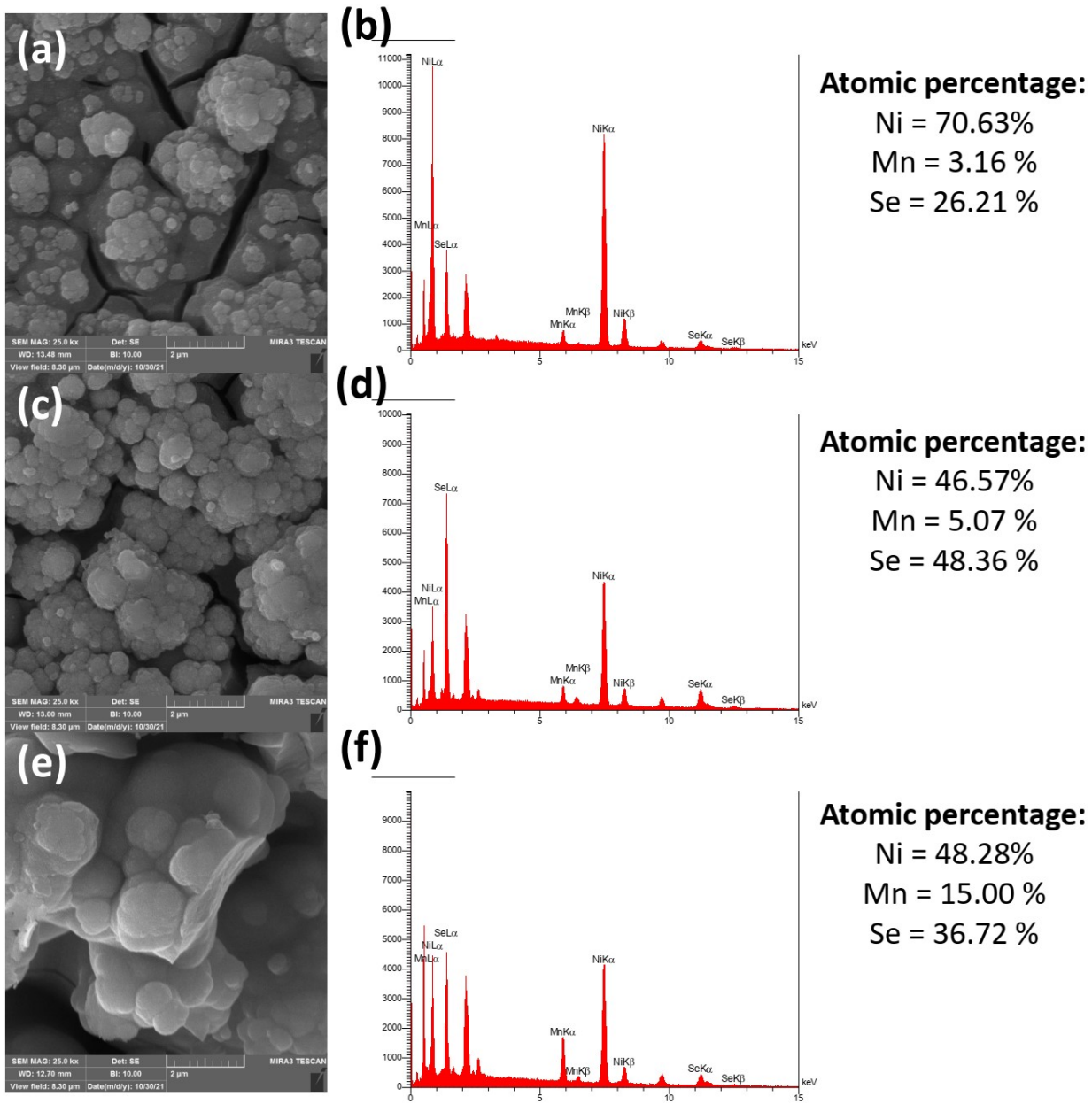$$\Delta G_{H*} = \Delta E_{H*} + \Delta E_{ZPE} - T\Delta S \qquad (8)$$

Where ΔE_{H*} is the hydrogen-binding energy, ΔE_{ZPE} is the differences in zero-point energy, and ΔS referred to the entropy changes as a result of hydrogen adsorption.
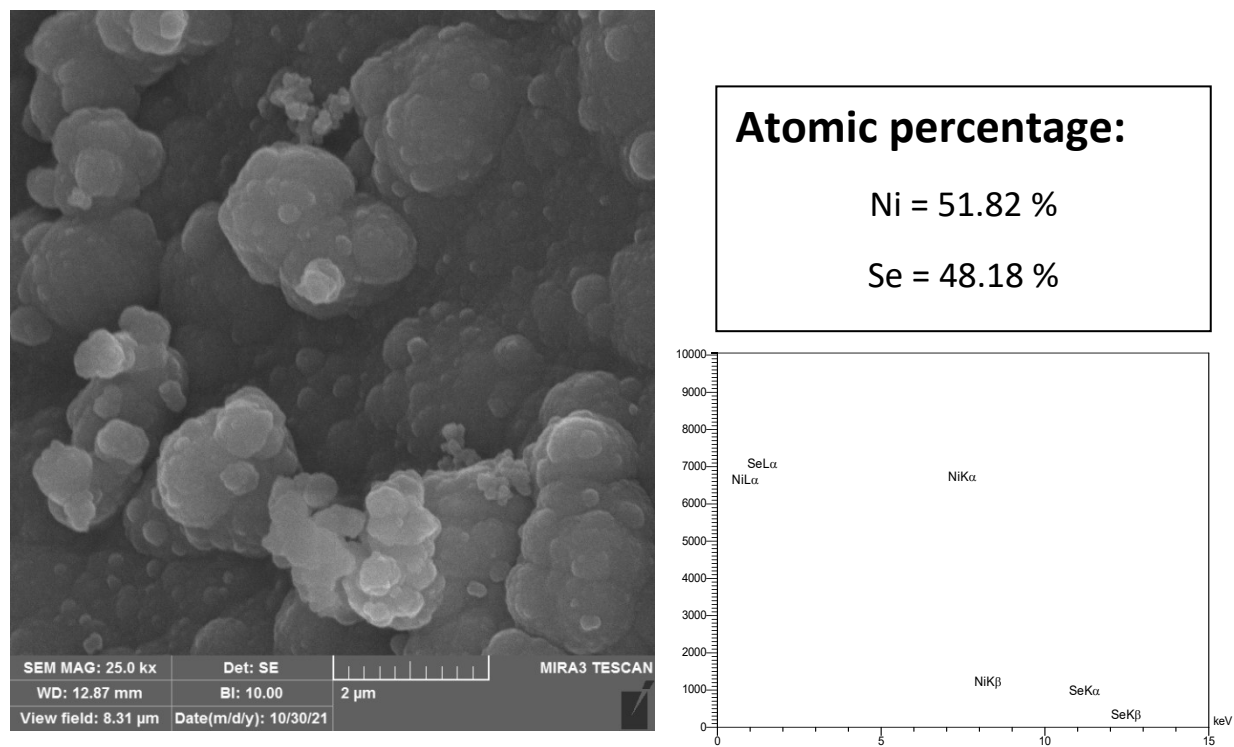
Figure S1. The FESEM image and EDS spectra of Ni-Se nanostructure.

Figure S2. TEM image of prepared Ni-Mn-Se electrode**.**

(a)

(b)

Atomic percentage:
Ni = 70.63%
Mn = 3.16 %
Se = 26.21 %

(c)

(d)

Atomic percentage:
Ni = 46.57%
Mn = 5.07 %
Se = 48.36 %

(e)

(f)

Atomic percentage:
Ni = 48.28%
Mn = 15.00 %
Se = 36.72 %

Figure S3. FESEM images and EDS spectra for prepared Ni-Mn-Se electrodes at **a,b** 5 min. **c,d** 10 min. **e,f** 30 min. Potential : -1.2 V vs. SCE.

Phase and chemical characterization

The phase characterizations of the Ni–Mn–Se and Ni–Se electrodes were performed using X-ray diffraction (XRD). As shown in Fig. S4, the XRD spectra of both samples have three peaks related to the Ni substrate due to the low coating thickness. The addition of Mn atoms in the Ni–Se shifts all of the peaks to lower degrees, which is in accordance with the Ni atoms being partially replaced by larger Mn atoms (inset Fig. S4). Further characterization of the optimized Ni–Mn–Se electrode by energy dispersive spectroscopy (EDS) revealed that the electrode consisted of Ni, Mn, and Se, and all elements are uniformly distributed on the surface according to the elemental mapping of the elements (Fig. S5). By inductively coupled plasma mass spectrometry (ICP–MS) analysis, the atomic ratio of 0.48 : 0.11 : 0.41 is confirmed for Ni, Mn, and Se in the Ni–Mn–Se electrocatalyst, respectively.

**Figure S4.** XRD pattern for prepared Ni-Mn-Se, and Ni-Se electrodes.
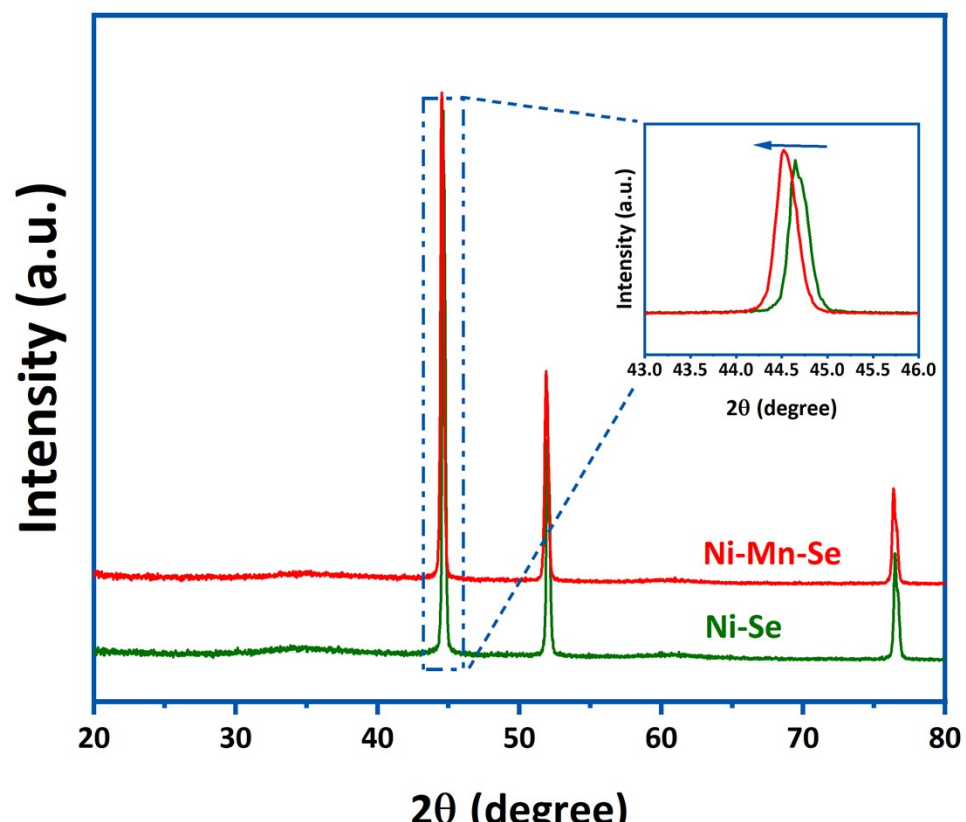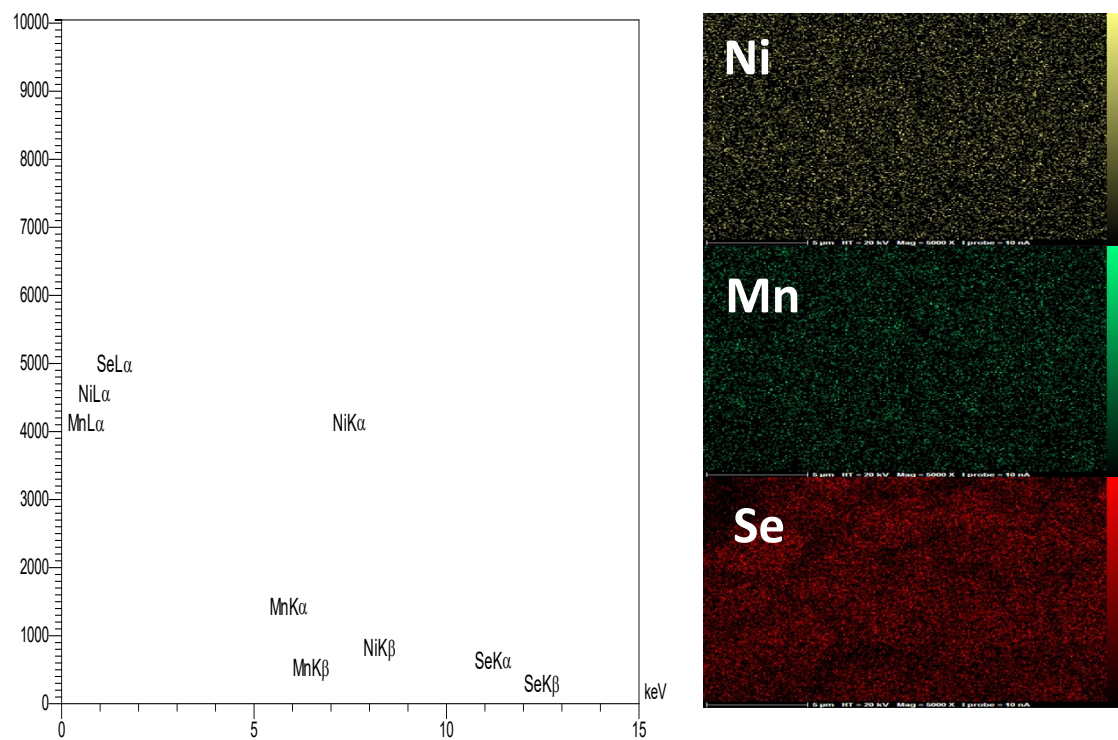
Figure S5. The EDS spectra and mapping of NiMnSe electrode.

**Finding optimized Ni-Mn-Se electrocatalyst**

Fig. S6a demonstrates the linear sweep voltammetric (LSV) curves of the Ni-Mn-Se samples for HER prepared in 5, 10, 20, and 30 minutes in 1.0 M KOH solution. The Ni-Mn-Se-20 sample has superior HER activities among all investigated Ni-Mn-Se samples by possessing overpotentials of 28 and 124 mV at current densities of -10 mA cm^{-2} and -200 mA cm^{-2}, which is lower than Ni-Mn-Se-5 (108 at -10 mA cm^{-2} and 320 at -200 mA cm^{-2}), Ni-Mn-Se-10 (93 at -10 mA cm^{-2} and 214 at -200 mA cm^{-2}), and Ni-Mn-Se-30 (46 at -10 mA cm^{-2} and 200 at -200 mA cm^{-2}). The Ni-Mn-Se-20 sample also exhibited higher reaction kinetics for HER by having a slight Tafel slope of 35.5 mV dec^{-1}, which is superior to Ni-Mn-Se-5 (141 mV dec^{-1}), Ni-Mn-Se-10 (81 mV dec^{-1}), Ni-Mn-Se-30 (49 mV dec^{-1}). The Double-Layer Capacitance (C_{dl}) values were also obtained to calculate the electrochemically active surface area (ECSA) of the different electrodes to analyze the effect of morphology of the as-prepared samples on the improvement of HER performance [1]. According to Fig. S6c, the Ni-Mn-Se-20 has the highest amount of C_{dl} (19.10 mF cm^{-2}), consequently has a larger ECSA, and provides more active sites for electrochemical reactions [2]. In line with the slight Tafel slope of the Ni-Mn-Se-20 sample, electrochemical impedance spectroscopy (EIS) measurements also revealed that the Ni-Mn-Se-20 sample has the lowest charge transfer resistance and consequently higher electrical conductivity than other samples (Fig. S6d), making the transfer of electrons much easier and expedites the reaction kinetics. The lower charge transfer resistance of Ni-Mn-Se-20 sample can be attributed to the optimum atomic percentage of incorporated Mn (12.11 at. %) that can tune the electronic structure of the host Ni-Se electrocatalyst. According to the obtained results, the optimal Ni-Mn-Se-20 sample was used as the target electrode to perform further electrochemical tests to evaluate its performance towards HER and UOR.
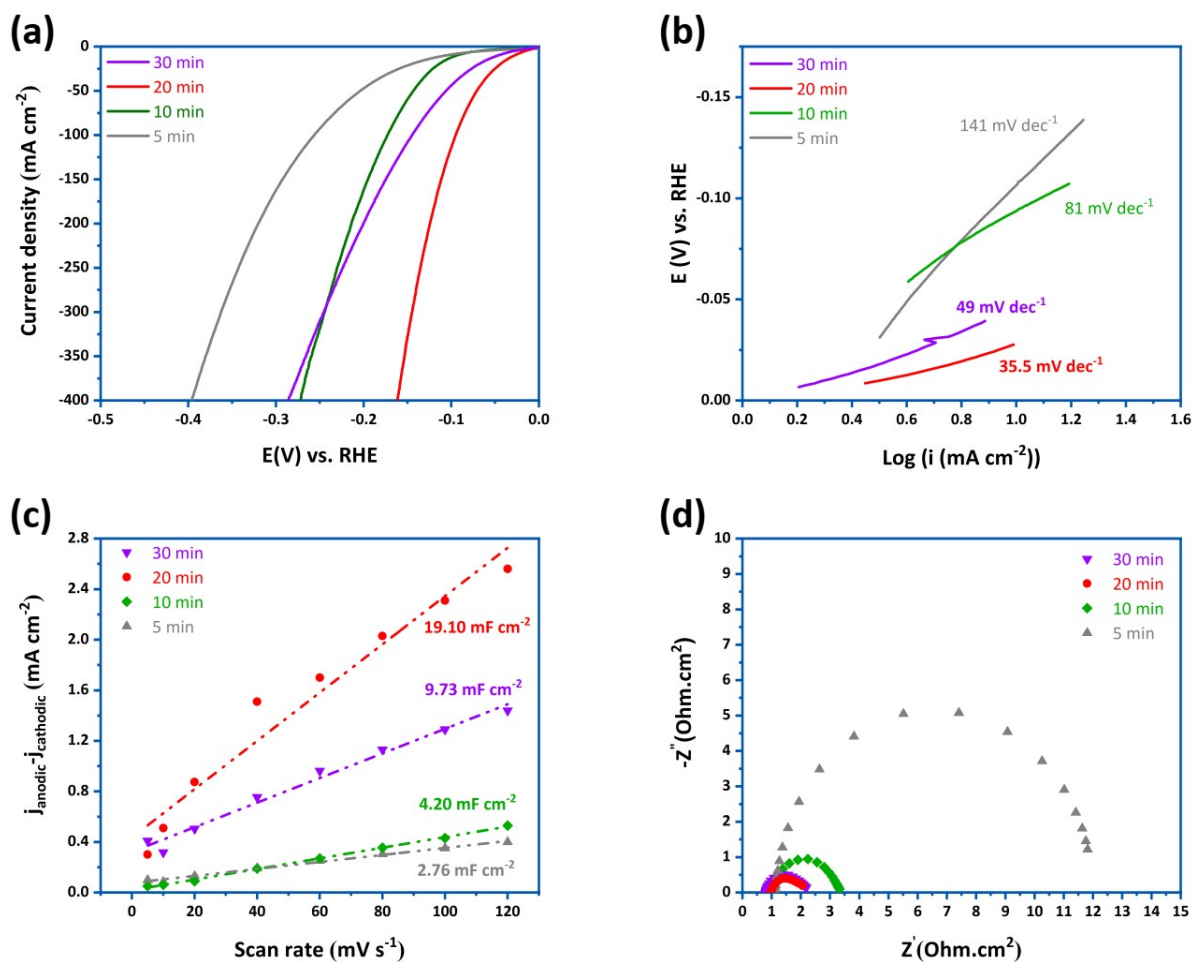
Figure S6. a-c Electrochemical performance for HER in 1.0 M KOH solution. **a** Polarization curves for the HER on prepared Ni-Mn-Se at different time. Sweep rate: 5 mV s^{-1}. **b** Tafel plots for catalysts derived from **a. c** plots showing the extraction of the C_{dl} for Ni-Mn-Se electrocatalysts. **d** Nyquist curves of electrodes prepared at 5 – 30 min.
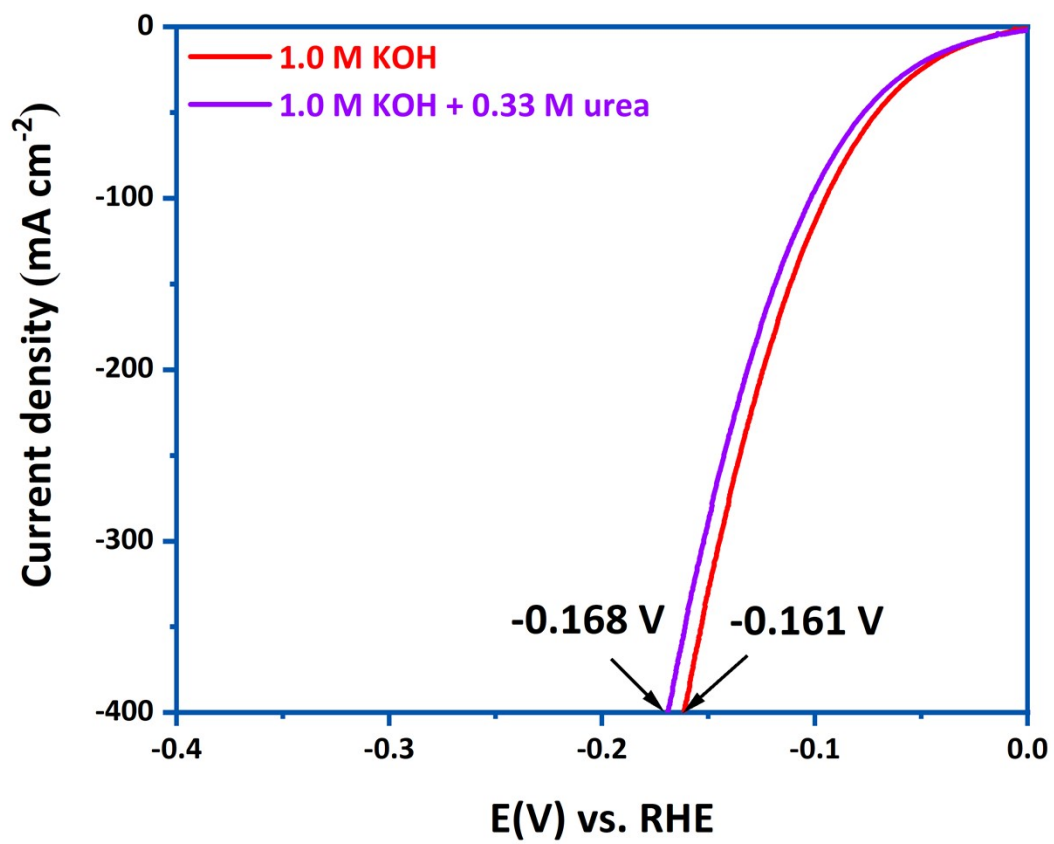
Figure S7. Polarization curves for the HER in 1.0 M KOH and 1.0 M KOH + 0.33 M urea solutions.
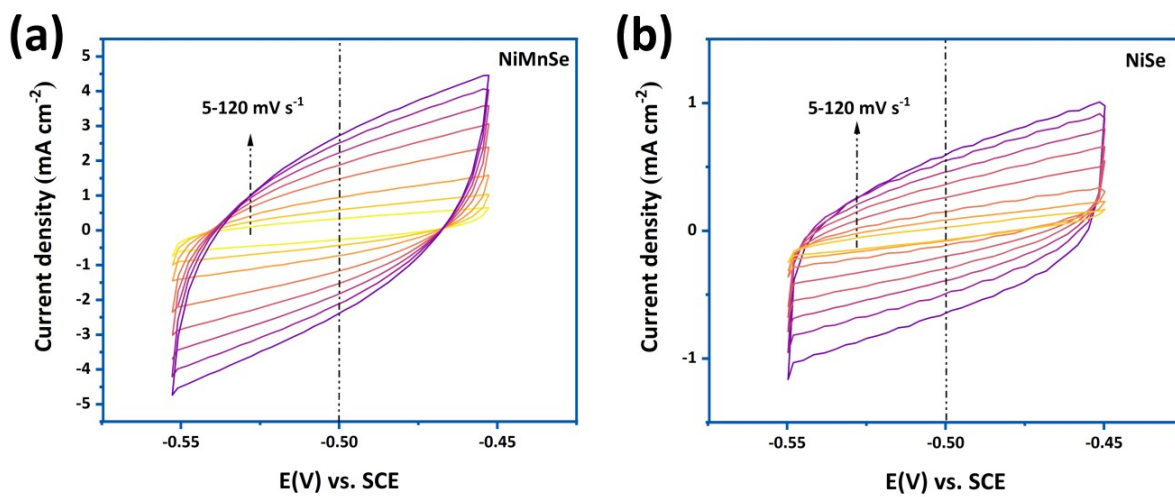
Figure S8. CV curves for **a** Ni-Mn-Se, **b** Ni-Se electrocatalysts.

Intrinsic catalytic activity

The turnover frequencies (TOFs) per surface site of catalysts were calculated to evaluate intrinsic catalytic activities for further investigation [3]. The calculated TOF value of Ni-Mn-Se is 1.21 s^{-1} at the overpotential of 150 mV (Fig. S10), which is higher than Ni-Se (0.197 s^{-1}). The tendency of TOF values is in full accordance with the intrinsic catalytic activity for HER, hinting that the considerably improved HER activity of Ni-Mn-Se is chiefly benefited from the synergistic catalytic effects caused by Mn atoms. Moreover, the LSV curves normalized by ECSA, as demonstrated in Fig. S9. It is found that Ni-Mn-Se indicates the better intrinsic activity. To deeper understand the effect of Mn atoms on the HER activity, density functional theory (DFT) calculations were performed (Fig. S11). The results demonstrate that the Mn incorporation brings about a decreasing trend in Gibbs free energy of hydrogen adsorption (ΔG_H*) from -0.407 eV for Ni-Se to -0.161 eV for Ni-Mn-Se electrode, which is further shows the role of Mn atoms as an electrochemical activity booster for Ni-Se electrocatalyst.
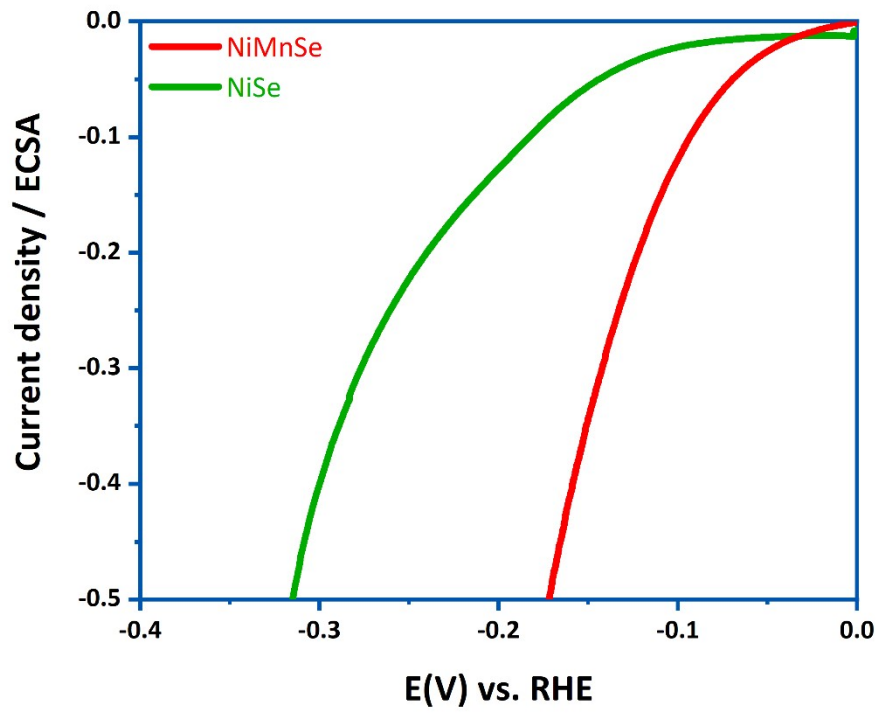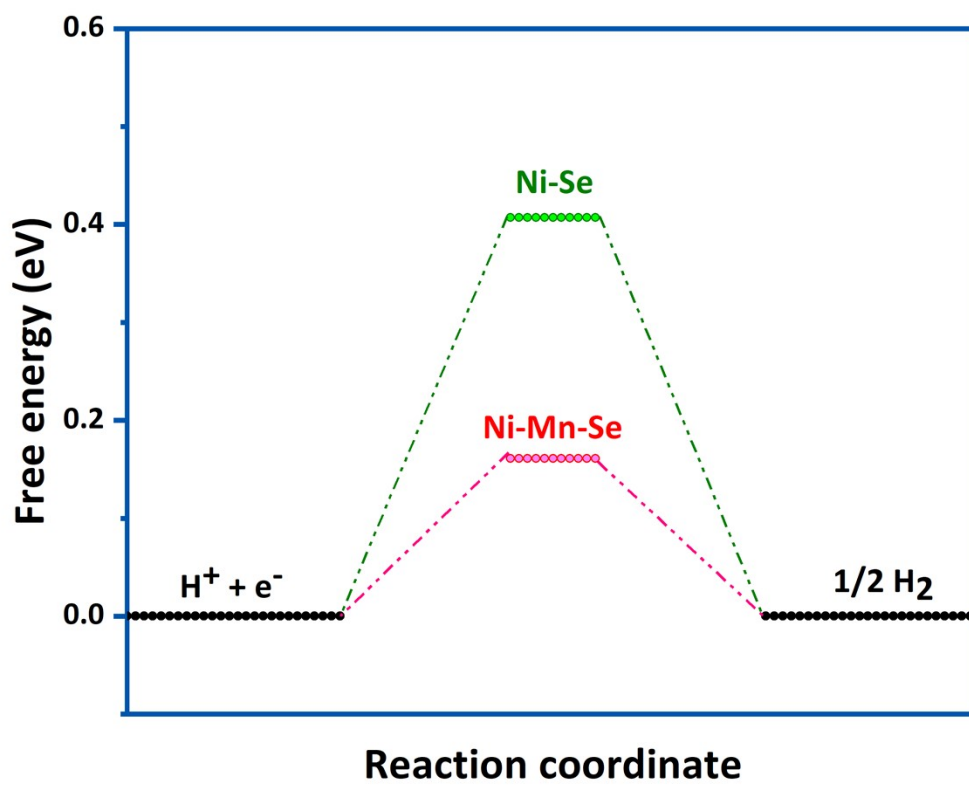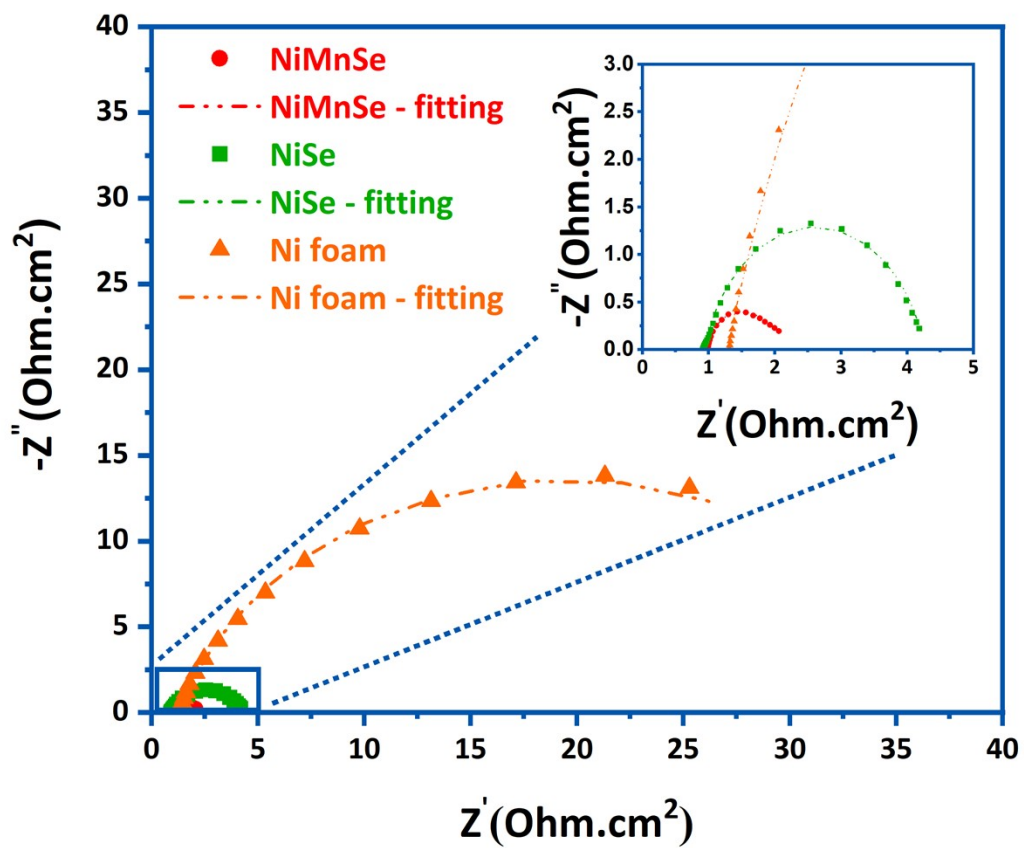
Figure S9. Normalized current densities to ECSA.
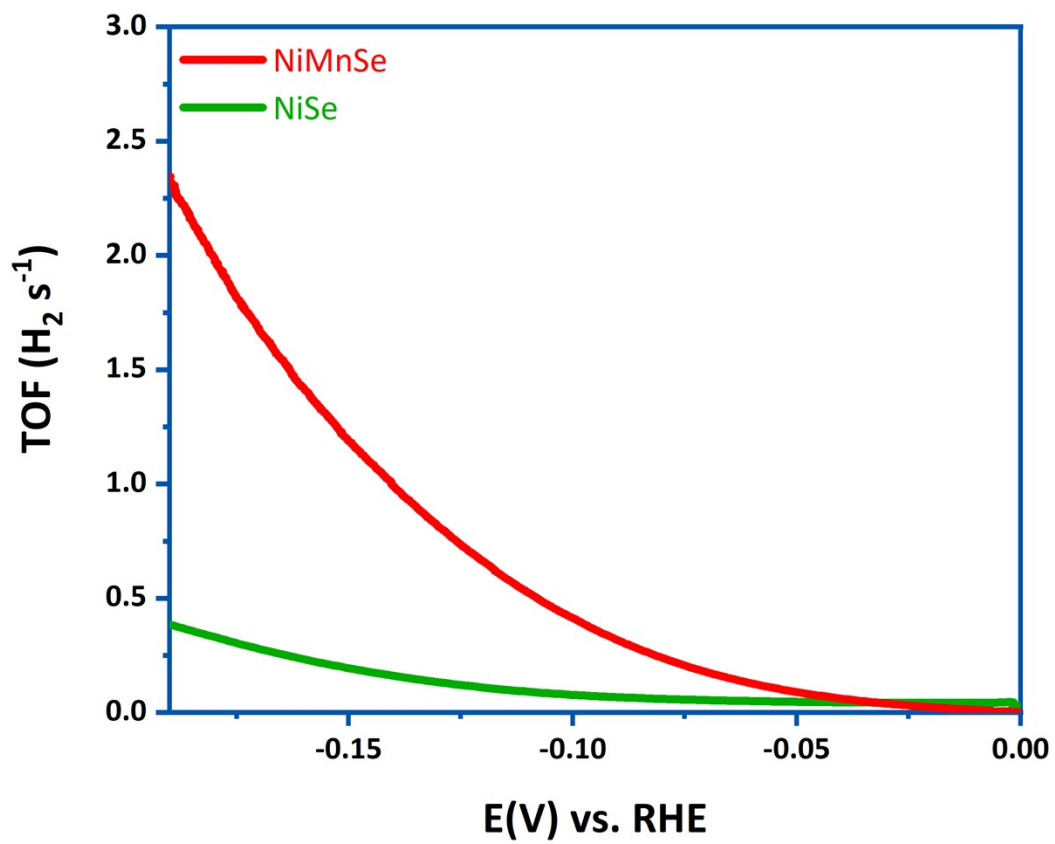
**Figure S10.** TOF plots for Ni-Mn-Se and Ni-Se electrocatalyst.

Figure S11. The Gibbs free energy of hydrogen adsorption calculated for Ni-Mn-Se and Ni-Se electrodes.
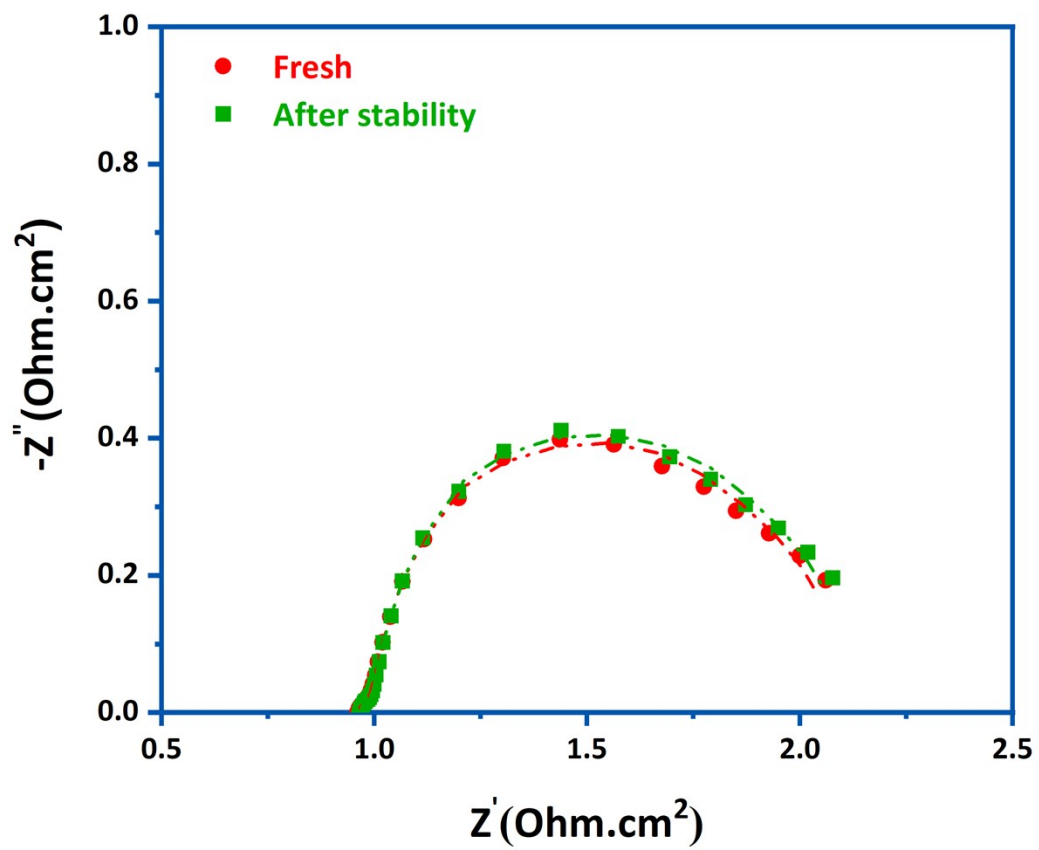
Figure S12. Nyquist curves of Ni-Mn-Se, Ni-Se, and Ni foam electrocatalysts in 1.0 M KOH electrolyte.
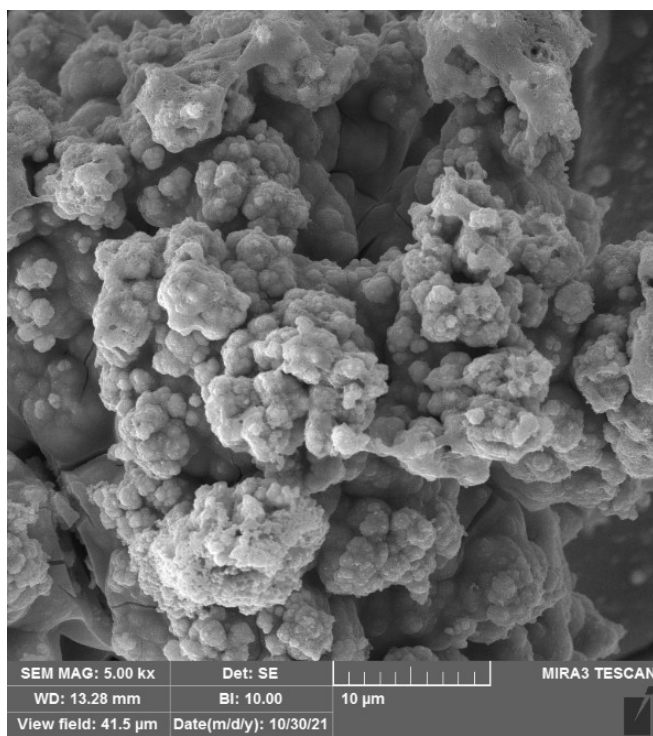
HER stability charactrisition

With the purpose of examining the HER stability of Ni-Mn-Se, multi-step chronopotentiometry and chronopotentiometry (Fig. S13) tests were performed at current densities of -50 to -300 mA cm^{-2}, and under a current density of -200 mA cm^{-2} for 50 hours, respectively, in 1.0 M KOH solution. Multi-step chronopotentiometry measurement exhibited outstanding mass transportation ability and mechanical robustness of Ni-Mn-Se, which exhibited that the potential of the electrodes remains almost constant at each step, and by varying the current density, the electrode potential changes rapidly. Also, during the chronopotentiometry test performed at a current density of -200 mA cm^{-2}, no significant potential change was observed over 50 hours (only 2.1% fluctuation). The EIS measurements (Fig. S14) and FESEM image (Fig. S15) show that charge transfer resistance and morphology of the Ni-Mn-Se remained almost constant even after 50h continues chronopotentiometry test.
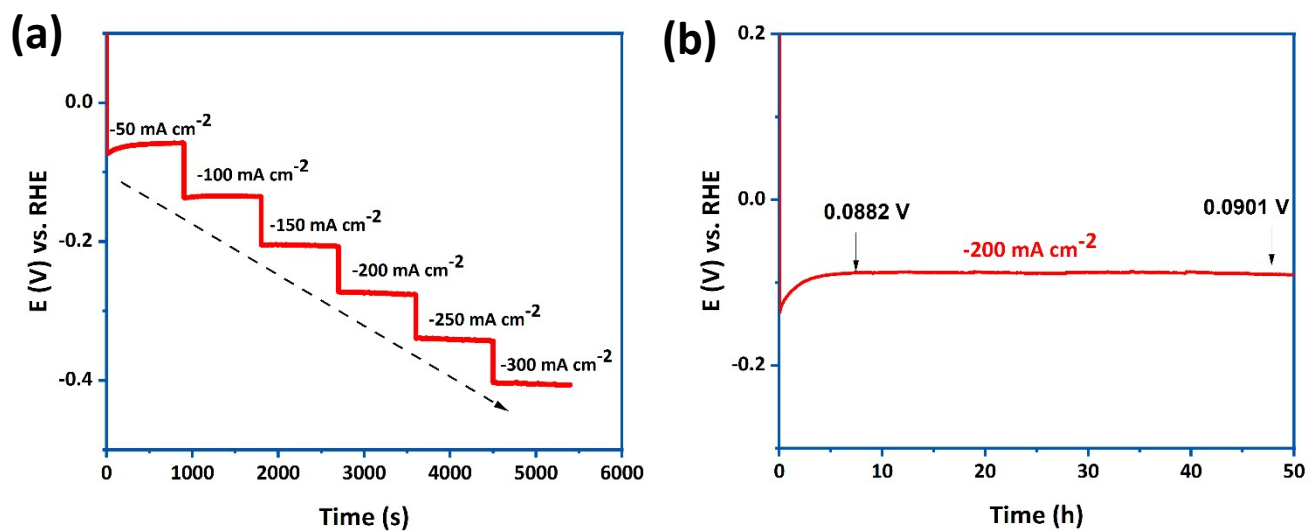
Figure S13. a Multi-step choronopotentiometry of NiMnSe electrocatalyst in 1.0 M KOH. **b** choronopotentiometry of NiMnSe electrocatalyst in 1.0 M KOH.

Figure S14. Nyquist curves of fresh and after HER stability NiMnSe electrocatalysts.
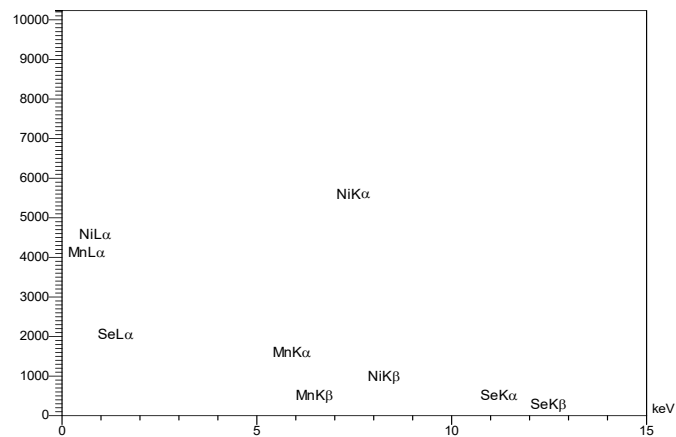
Atomic percentage:

Ni = 68.83 %

Mn = 10.12 %

Se = 21.04 %

Figure S15. The FESEM image and EDS spectra of NiMnSe electrocatalyst after HER stability.

UOR and cell stabilty charactrizations

For investigating the stability of UOR performance of Ni-Mn-Se, multi-step chronopotentiometry (Fig. 4d) and chronopotentiometry (Fig. S16a) tests were performed at current densities of 50 to 300 mA cm^{-2} under a current density of 200 mA cm^{-2} for 50 hours in 1.0 M KOH + 0.33 M urea solution. As with the Ni-Mn-Se stability results in HER, the Ni-Mn-Se electrode performed very well in the UOR and maintained its stability by drastically changing the current density at each step. Similarly, during 50 hours, the continuous performance of the UOR of the Ni-Mn-Se electrode at a high current density of 200 mA cm^{-2} showed negligible potential fluctuation of 1.22 %. The EIS measurements (Fig. S17) and FESEM image (Fig. S18) show that electron conductivity and morphology of the Ni-Mn-Se remained the same after 50 h continues UOR chronopotentiometry test. Fig. S15b also demonstrates the chronopotentiometry results of the Ni-Mn-Se as a bi-functional electrocatalyst for urea electrolysis stability evaluation during 50 hours at a fixed current density of 50 mA cm^{-2}. As it is clear, the optimal Ni-Mn-Se electrode during the chronopotentiometry test was able to show extremely stable and durable performance with only 0.19% fluctuation.
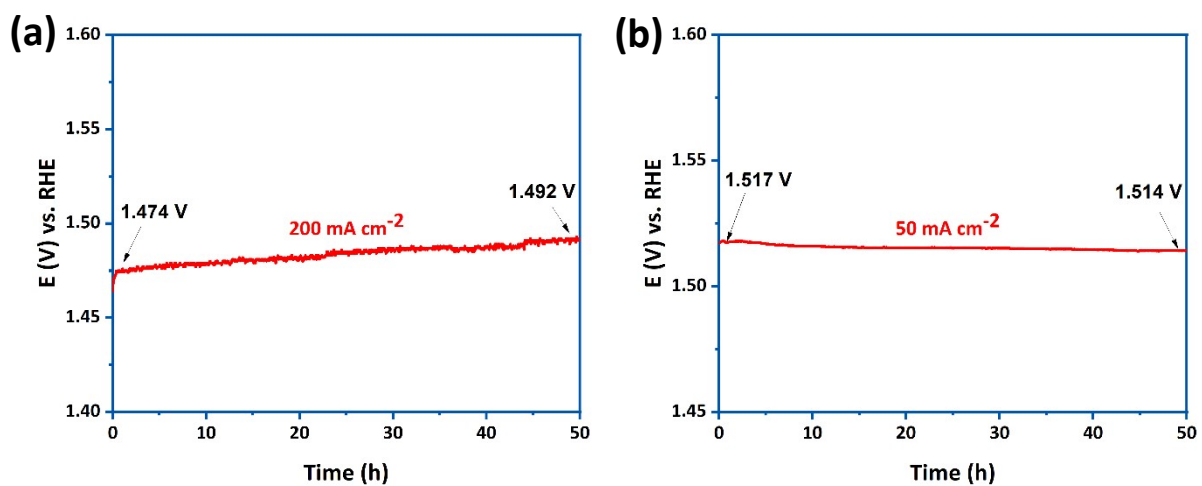
Figure S16. a UOR choronopotentiometry of NiMnSe electrocatalyst in 1.0 M KOH + 0.33 M urea. **b** Cell choronopotentiometry of NiMnSe electrocatalyst in 1.0 M KOH + 0.33 M urea.
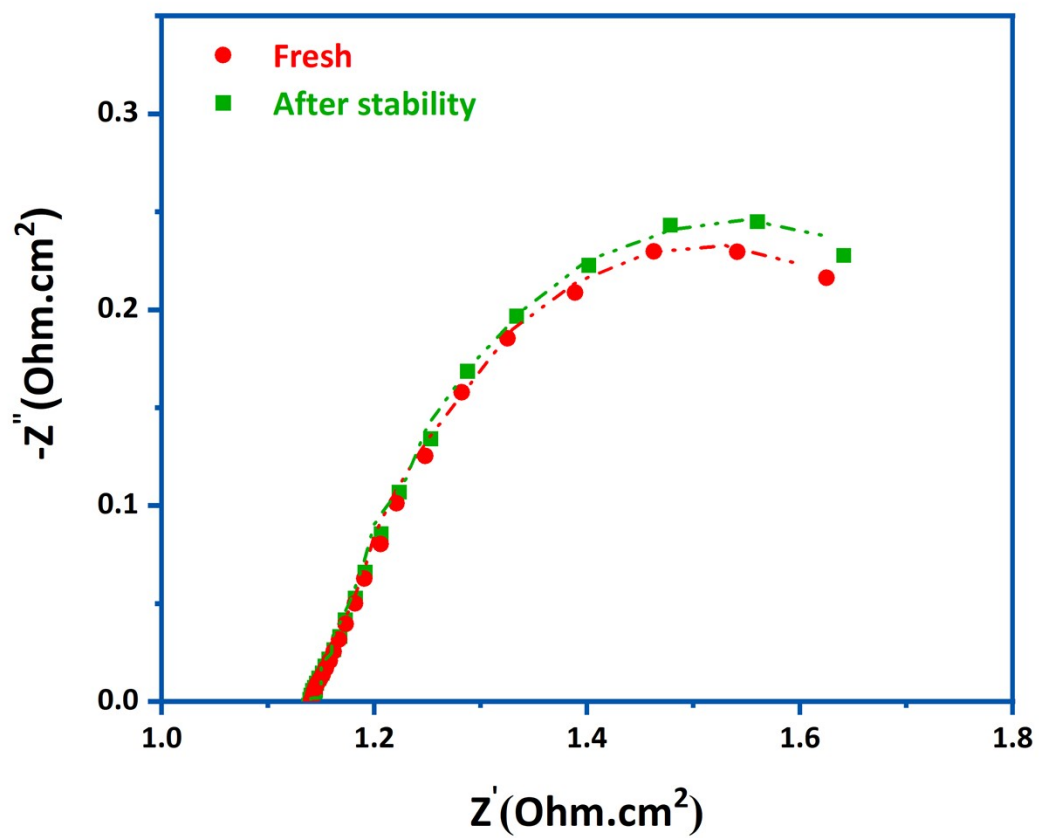
Figure S17. Nyquist curves of fresh and after HER stability NiMnSe electrocatalysts.
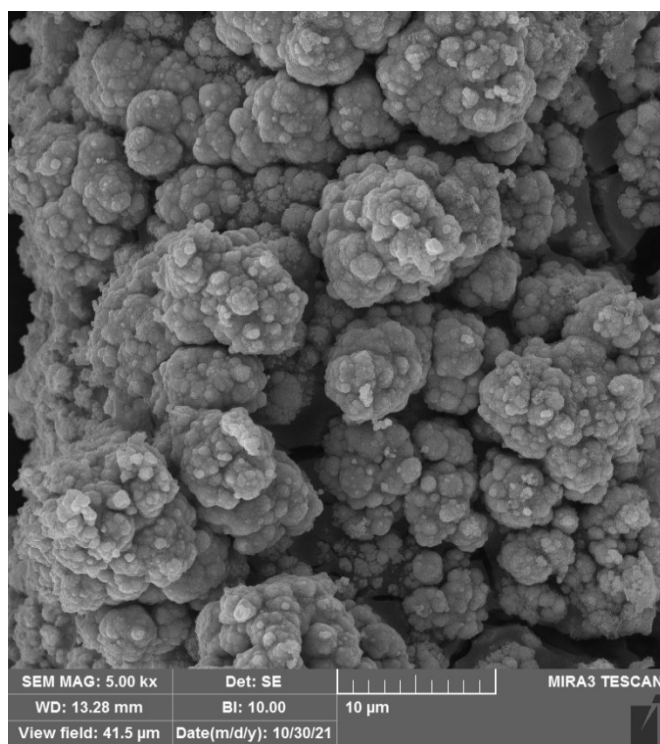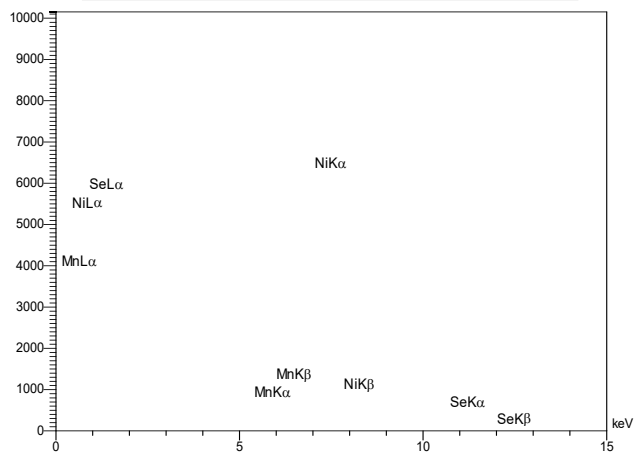
Atomic percentage:

Ni = 59.96 %

Mn = 3.85 %

Se = 36.18 %

Figure S18. The FESEM image and EDS spectra of NiMnSe electrocatalyst after UOR stability.

Table S1. Comparison of catalytic parameters of Ni-Mn-Se and other non-noble-metal HER electrocatalysts.

Preparation method	Catalyst composition	Electrolyte	Her over-potential at the corresponding j (mV \\ mA.cm^{-2})	Tafel slope (mV.dec^{-1})	Stability (hours)	Refs
Electrodeposition	Ni-Mn-Se/NF	1 M KOH	28 \\ 10 95 \\ 100 (1570 \\ 10 cell)	35.5	50	This work
Hydrothermal	Mn-Ni$_3$S$_2$/NF	1 M KOH	152 \\ 10	98	20	[4]
Electrodeposition	Mn-Co-P/Ti	1 M KOH	76 \\ 10	55	10	[5]
Hydrothermal and chemical deposition treatments	Se-doped MnS/NiS	1 M KOH	56 \\ 10	55	48	[6]
Solvothermal	Mn-NiSe$_2$/carbon fiber	0.5 M H$_2$SO$_4$	86 \\ 10	59	20	[7]
Thermal	MnSe$_2$/CoSe$_2$	1 M KOH	1660 \\ 50 (cell)	93	-	[8]
Hydrothermal	Mn-Ni$_2$P/NF	1 M KOH	103 \\ 20	135	25	[9]
Hydrothermal	Mn-NiP$_2$ NSs/CC	1 M KOH 0.5 M H$_2$SO$_4$	97 \\ 10 69 \\ 10	45	20	[10]
Thermal	Mn-FeP	1 M KOH 0.5 M H$_2$SO$_4$	173 \\ 10 69 \\ 10	95	10	[11]
Electrodeposition	Co$_{0.13}$Ni$_{0.87}$Se$_2$/Ti	1 M KOH	64 \\ 10 (1620 \\ 10 cell)	63	60	[12]
Hydrothermal	NiMn$_{1.5}$PO$_4$/NF	1 M KOH	72 \\ 10	43	50	[13]
Hydrothermal	Mn-doped NiCoP	1 M KOH 0.5 M H$_2$SO$_4$	67 \\ 10 37 \\ 10	-	120	[14]
Hydrothermal	Mn-MoP	1 M KOH 0.5 M H$_2$SO$_4$	198 \\ 10 199 \\ 10	50 49	50	[15]
Coprecipitation method and annealing	CoMn-P@NG	1 M KOH 0.5 M H$_2$SO$_4$	190 \\ 20 159 \\ 20	110.69 64.85	12	[16]
Electrochemical reduction	Mn-CoP@ Mn-CoOOH	1 M KOH	110 \\ 10	54	-	[17]

Table S2. Comparison of cell voltage of Ni-Mn-Se‖Ni-Mn-Se and other non-noble-metal electrocatalysts in 1.0 M KOH and 1.0 M KOH + 0.33 urea solutions.

Preparation method	Catalyst composition	Electrolyte	Cell voltage at the corresponding j (mV \\ mA.cm^{-2})	Refs
electrodeposition	Ni-Mn-Se/NF	1 M KOH + 0.33 M KOH	1352 \\ 10 1620 \\ 100	This work
Ultrasonic/heating-assisted activation strategy	Ni(OH)$_2$@NF	1 M KOH + 0.33 M urea	1350 \\ 10	[18]
Thermal	Ni$_3$N/NF	1 M KOH + 0.5 M urea	1400 \\ 100	[19]
Hydrothermal	F-Ni$_3$S$_2$/NF	1 M KOH + 0.33 M urea	1360 \\ 50	[20]
Hydrothermal + annealing	NF/NiMoO-Ar	1 M KOH + 0.5 M urea	1370 \\ 10	[21]
Hydrothermal	Ni$_9$S$_8$/CuS/Cu$_2$O/NF	1 M KOH + 0.33 M urea	1470 \\ 10	[22]
Hydrothermal + annealing	FeNi$_3$-MoO$_2$/NF	1.0 M KOH + 0.5 M urea	1370 \\ 10	[23]
Wet-chemical + phosphorization	CoP/C-3	1 M KOH + 0.1 M urea	1400 \\ 10	[24]
Hydrothermal	Ni$_3$S$_2$@NF	1.0 M NaOH + 0.33 M urea	1490 \\ 20	[25]
preparation	Ni$_{0.7}$Fe$_{0.3}$	1.0 M KOH + 0.33 M urea	1550 \\ 10	[26]
Hydrothermal and sulfuration processes	CoS2 NA/Ti mesh	1.0 M KOH + 0.3 M urea	1590 \\ 10	[27]
Hydrothermal reaction	MoS$_2$/Ni$_3$S$_2$/NiFe-LDH	1.0 M KOH + 0.5 M urea	1343 \\ 50	[28]

co-infiltration - thermal reduction	$Ni_{(10\%)}Pd_{(10\%)}/$ OMC	1 M KOH +0.33 M urea	1350 \\ 30	29

References

1   G. Wang, J. Chen, P. Cai, J. Jia and Z. Wen, *Journal of Materials Chemistry A*, 2018, **6**, 17763–17770.

2   Y. Tan, Y. Yin, X. Yin, C. Lan, Y. Wang, F. Hu, Q. Huang and Y. Mi, *Catalysts*, 2021, **11**, 1–13.

3   L. Yan, B. Zhang, J. Zhu, Y. Li, P. Tsiakaras and P. Kang Shen, *Applied Catalysis B: Environmental*, 2020, **265**, 118555.

4   H. Du, R. Kong, F. Qu and L. Lu, *Chemical Communications*, 2018, **54**, 10100–10103.

5   T. Liu, X. Ma, D. Liu, S. Hao, G. Du, Y. Ma, A. M. Asiri, X. Sun and L. Chen, *ACS Catalysis*, 2017, **7**, 98–102.

6   J. Zhu, M. Sun, S. Liu, X. Liu, K. Hu and L. Wang, *Journal of Materials Chemistry A*, 2019, **7**, 26975–26983.

7   X. Wang, H. Tian, M. Pi, D. Zhang and S. Chen, *International Journal of Hydrogen Energy*, 2020, **45**, 12237–12243.

8   G. Mei, H. Liang, B. Wei, H. Shi, F. Ming, X. Xu and Z. Wang, *Electrochimica Acta*, 2018, **290**, 82–89.

9   Y. Zhang, Y. Liu, M. Ma, X. Ren, Z. Liu, G. Du, A. M. Asiri and X. Sun, *Chemical Communications*, 2017, **53**, 11048–11051.

10   X. Wang, H. Zhou, D. Zhang, M. Pi, J. Feng and S. Chen, *Journal of Power Sources*, 2018, **387**, 1–8.

11   M. Wang, Y. Tuo, X. Li, Q. Hua, F. Du and L. Jiang, *ACS Sustainable Chemistry and Engineering*, 2019, **7**, 12419–12427.

12   T. Liu, A. M. Asiri and X. Sun, *Nanoscale*, 2016, **8**, 3911–3915.

13   G. Zhang, H. Ge, L. Zhao, J. Liu, F. Wang, S. Fan and G. Li, *Electrochimica Acta*, 2021, **367**, 137567.

14   X. Yu, S. Xu, Z. Wang, X. Cheng, Y. Du, G. Chen, X. Sun and Q. Wu, *Nanoscale*.

15   Z. Mu, T. Guo, H. Fei, Y. Mao, Z. Wu and D. Wang, *Applied Surface Science*, 2021, **551**, 149321.

16   J. Liu, W. Li, Z. Cui, J. Li, F. Yang, L. Huang, C. Ma and M. Zeng, *Chemical Communications*, 2021, **57**, 2400–2403.

17   X. Li, Q. Hu, H. Wang, M. Chen, X. Hao, Y. Ma, J. Liu, K. Tang, A. Abudula and G. Guan, *Applied Catalysis B: Environmental*, 2021, **292**, 120172.

18   L. Xia, Y. Liao, Y. Qing, H. Xu, Z. Gao, W. Li and Y. Wu, *ACS Applied Energy Materials*, , DOI:10.1021/acsaem.0c00122.

19   S. Hu, C. Feng, S. Wang, J. Liu, H. Wu, L. Zhang and J. Zhang, *ACS Applied Materials and Interfaces*, 2019, **11**, 13168–13175.

20   P. Hao, W. Zhu, F. Lei, X. Ma, J. Xie, H. Tan, L. Li, H. Liu and B. Tang, *Nanoscale*, 2018, **10**, 20384–20392.

21   Z. Y. Yu, C. C. Lang, M. R. Gao, Y. Chen, Q. Q. Fu, Y. Duan and S. H. Yu, *Energy and Environmental Science*, 2018, **11**, 1890–1897.

22   D. Wei, W. Tang and Y. Wang, *International Journal of Hydrogen Energy*, 2021, **46**, 20950–20960.

23   Q. Xu, T. Yu, J. Chen, G. Qian, H. Song, L. Luo, Y. Chen, T. Liu, Y. Wang and S. Yin, *ACS Applied Materials and Interfaces*, 2021, **13**, 16355–16363.

24   J. Zheng, K. Wu, C. Lyu, X. Pan, X. Zhang, Y. Zhu, A. Wang, W. M. Lau and N. Wang, *Applied Surface Science*, 2020, **506**, 144977.

25   M. Liu, Y. Jiao, S. Zhan and H. Wang, *Catalysis Today*, 2020, **355**, 596–601.

26   Z. Cao, T. Zhou, X. Ma, Y. Shen, Q. Deng, W. Zhang and Y. Zhao, *ACS Sustainable Chemistry and Engineering*, 2020, **8**, 11007–11015.

27   S. Wei, X. Wang, J. Wang, X. Sun, L. Cui, W. Yang, Y. Zheng and J. Liu, *Electrochimica Acta*, 2017, **246**, 776–782.

28   M. He, S. Hu, C. Feng, H. Wu, H. Liu and H. Mei, *International Journal of Hydrogen Energy*, 2020, **45**, 23–35.

29   N. Muthuchamy, S. Jang, J. C. Park, S. Park and K. H. Park, *ACS Sustainable Chemistry and Engineering*, 2019, **7**, 15526–15536.